Constructing an Expandable Molecular Chain as a Functionalized Flexible Matrix to Achieve Lithium-Free Anode

Jiaqing Cui[+],[a] Kun Wang[+],[a] Yapeng Shi[+],[a] Xinxin Yang,[a] Ruming Yuan,[a] Jingmin Fan,[a] Mingsen Zheng,*[a] and Quanfeng Dong*[a]

Lithium metal has been considered the most ideal choice for the anode in rechargeable high energy density batteries. Direct metal anode is a plating/stripping process without any self-supporting framework, thus making the metal electrodes susceptible to collapse and difficult for the repeating processes. Herein, we construct a stretchable molecular chain as a flexible skeleton to achieve the lithium repeated plating/stripping. The $Cu_xS\text{-}In_2S_3$ can in situ be converted into lithiophilic LixIny and Li_2S composites during the lithium deposition process in which an "expandable molecule chains" is formed through the S connections. Once formed, the lithiophilic chains remain existing stable but just their upright state changes thus serving as a functionalized flexible matrix (FFM) for the lithium dissolution and deposition process. Benefiting from these features, the anode-free full cells FFM‖LFP display superior cycling stability and long lifespan, with a high-capacity retention of 86.7% at 0.2 C-rate after 100 cycles. These explorations provide new strategies for developing high-performance 'Anode-free' lithium metal battary (AFLMB).

Introduction

With the increasing demand for high-energy-density rechargeable technologies, traditional lithium-ion batteries (LIBs) based on intercalation chemistry have proven insufficient.[1,2] Due to the ultrahigh theoretical capacity (3860 mAh g^{-1}), low redox potential (-3.04 V vs. standard hydrogen electrode), and low gravimetric density (0.534 g cm^{-3}) of lithium metal anode (LMA),[3–6] lithium metal battery (LMB) is considered among the most promising candidates.[7–9] From an alternative perspective on battery design, lithium metal electrodes can be regarded as supplementary lithium sources, as the Li$^+$ participating in plating/stripping reactions originate from the cathode. Although a certain amount of extra lithium source is necessary due to the poor reversibility of the Li plating/stripping process, the ideal configuration for maximizing the energy density of LMBs is an anode without lithium metal, which is called anode-free lithium metal battery (AFLMB).[10–13]

To enhance capacity and cycling stability in AFLMB, various strategies for stabilizing lithium deposition have been investigated, including innovative electrolyte formulations,[14–19] artificial solid electrolyte interphase (SEI) layers,[20–25] and modified current collector substrates.[26–33] In particular, lithiophilic metals that can form binary or multinary alloy phases with lithium have attracted extensive attention from researchers and have been proven to be effective in regulating lithium deposition behavior. But these strategies primarily focus on the external regions of the electrode, specifically the electrode/electrolyte interface and the electrode/substrate interface,[34,35] which are crucial during the initial stages of lithium deposition. However, as lithium dissolution and precipitation cycles repeat and the volume of lithium deposition increases, the effectiveness of these surface modification strategies diminishes.[36,37] They are insufficient to address the issues arising from the uncontrollable growth of lithium dendrites and the inevitable volume fluctuations,[38] which ultimately result in low Coulombic efficiency (CE) and a reduced lifespan for AFLMB. Therefore, to effectively regulate the lithium plating/stripping process on the electrode, it is essential to establish an intrinsic framework that supports the lithium anode in achieving a long-term repeated plating/stripping process.

In this work, we developed a stretchable molecular chain to serve as a functionalized flexible matrix (FFM) aimed at achieving an alternative lithium plating/stripping process inside electrode (Figure 1). Firstly, In_2S_3 and CuS were effectively fabricated on the surface of a copper net using electrochemical deposition and chemical vapor deposition (CVD) techniques. Then the FFM can be converted into lithiophilic LixIny and Li_2S during the lithium deposition process, forming the "expandable molecule chains " inside electrode through sulfur connections. Once formed, the lithiophilic chains will persistently exist on the

[a] J. Cui,[+] K. Wang,[+] Y. Shi,[+] X. Yang, R. Yuan, J. Fan, M. Zheng, Q. Dong
Department of Chemistry, College of Chemistry and Chemical Engineering, Xiamen University
State Key Laboratory of Physical Chemistry of Solid Surfaces and Department of Chemistry, College of Chemistry and Chemical Engineering, Xiamen University
and
Engineering Research Center of Electrochemical Technology, College of Chemistry and Chemical Engineering, Xiamen University
Innovation Laboratory for Sciences and Technologies of Energy Materials of Fujian Province (IKKEM), Xiamen, China
E-mail: mszheng@xmu.edu.cn
        qfdong@xmu.edu.cn
[+] These authors contributed equally to this work.
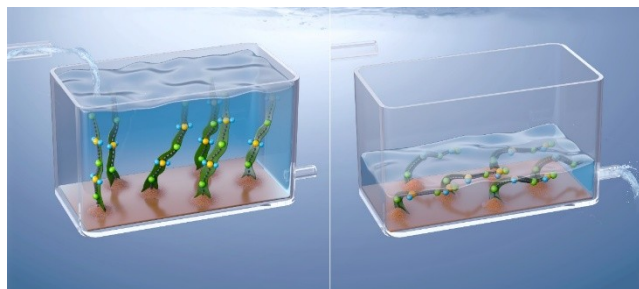🖳 Supporting information for this article is available on the WWW under https://doi.org/10.1002/batt.202500033

Batteries & Supercaps

Research Article
doi.org/10.1002/batt.202500033

Chemistry Europe
European Chemical
Societies Publishing

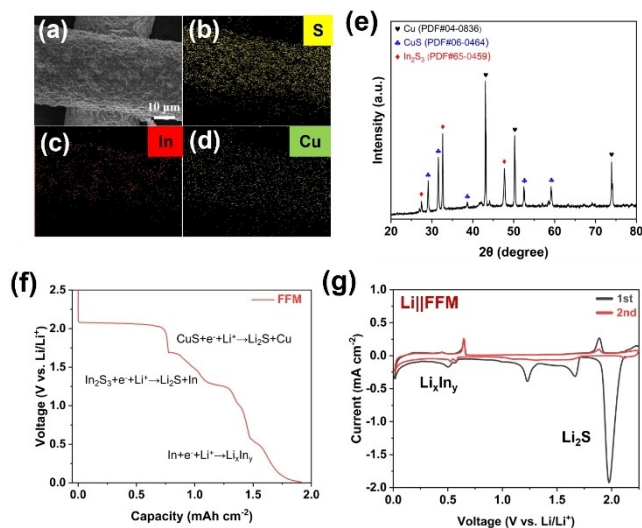**Figure 1.** Scheme of the Li plating and stripping process on FFM.

Figure 2. SEM image of FFM a) and Mapping images of FFM, b) S, c) In and d) Cu. e) XRD pattern of FFM. f) Voltage-capacity plots of FFM after initial discharge to 0.01 V at a current density of 0.1 mA cm^{-2} g) The cyclic voltammograms experiment of FFM at a scan rate of 0.1 mV s^{-1} between 0.01 V and 2.25 V.

substrate, with only their upright state changes during the lithium dissolution and deposition process thus serving as a functionalized flexible matrix (FFM) to self-supporting Li plating/stripping with high reversibility. Benefiting from these attributes, the FFM-based lithium-free anode (Li@FFM) exhibits impressive Coulombic efficiency and remarkably improved cycle stability of AFLMB in conventional carbonate-based electrolyte.

Results and Discussion

The fabrication process of the Cu_xS-In_2S_3-modified collector is schematically presented in Figure S1 (Supporting Information). First, indium metal was uniformly deposited on the surface of the Cu net (denoted as Cu net-In) using a simple electrodeposition method. After washing with deionized water and anhydrous ethanol, and drying in ambient air, the Cu net-In was annealed at 210 °C for 2 h under a mixed Ar and sulfur vapor atmosphere to partially sulfurize the Cu net-In to obtain FFM. The morphology changes of the Cu net at different stages were characterized by scanning electron microscopy (SEM). After the electrodeposition process, the metal indium coating was smooth and conformal on the surface of the Cu net (Figure S2a, Supporting Information). After the sulfurization process, the morphology of FFM (Figure S2b, Supporting Information) exhibits uniformity and density. The corresponding element mappings of the SEM image reveal the homogeneous dispersion of S, In and Cu elements in the coating layer (Figure 2a–d). Moreover, the energy dispersive spectrometer (EDS) image in Figure S3 (Supporting Information) confirmed the element composition (In, S and Cu) after the electrodeposition and sulfurization process.

The X-ray diffraction (XRD) patterns in Figure 2e display the typical In_2S_3 peaks located at 27.6°, 32.6° and 47.7°, which are assigned to the (311), (400) and (440) lattice planes of In_2S_3 (JCPDS 65-0459). Additionally, the CuS peaks were located at 29.2°, 32.8°, 38.8°, 52.7° and 59.3°, corresponding to the (102), (006), (105), (108) and (116) lattice planes of CuS (JCPDS 06–0464). The other peaks are attributed to the lattice planes of (111), (200) and (220) of the Cu substrate (JCPDS 04-0836). The X-ray photoelectron spectroscopy (XPS) characterization of FFM is presented in Figure S4 (Supporting Information). The two peaks at 452.1 and 444.5 eV are attributed to the binding energies of In $3d_{3/2}$ and In $3d_{5/2}$, respectively, while the two

peaks at 952.3 and 932.5 eV correspond to Cu $2p_{1/2}$ and Cu $2p_{1/2}$. The distance between these two peaks is approximately 7.6 and 19.8 eV, respectively. Combined with the XRD analysis mentioned above, this confirms the presence of In_2S_3 and CuS on the Cu net substrate.

In addition, during the initial activation process (galvanostatic discharge to 0.01 V, Figure 2f), the discharge plateau appears at 2.1 V and 1.7 V, corresponding to the lithiation process that leads to CuS being converted to Cu and Li_2S, and In_2S_3 being converted to In and Li_2S. Furthermore, the discharge plateau between 0.6 V and 0.1 V indicates the transformation process of LixIny compounds, which can be compared with the lithiation process of Cu net-In (Figure S5, Supporting Information), showing only the transfer process of LixIny on the Cu net substrate. The redox peaks in the cyclic voltammograms of FFM (Figure 2g) also correspond to the characteristic plateau observed in the lithium deposition curve mentioned above. It can be noted that the Li_2S peak appeared in the first cycle but disappeared in the second cycle, indicating that Li_2S can stably exist after initial activation. The redox peaks of LixIny persist, indicating that the transformation process of LixIny continues with the deposition and stripping of lithium, which can also be observed on Cu net-In with only indium metal coating (Figure S6, Supporting Information). The XRD spectra in Figure 3a reveal the characteristic peaks of Li_2S and LixIny within the Li@FFM electrode, and the composition of the surface coating relative to the inner layer was further explored by obtaining the Li 1s, S 2p and In 3 d XPS depth profiles in Figure 3b–d after sequentially Ar$^+$ sputtering. The intensity of the characteristic peak of Li_2S (54.1 eV in Li 1s spectra; 160.1 and 161.3 eV in S 2p spectra) gradually increased, particularly after 20 s of Ar$^+$ sputtering, where Li_2S replaced Li_2CO_3 (55.1 eV in Li 1s spectra) and LiOR (54.7 eV in Li 1s spectra) as the dominant component of the intrinsic. Notably, compared with common SEI compo-
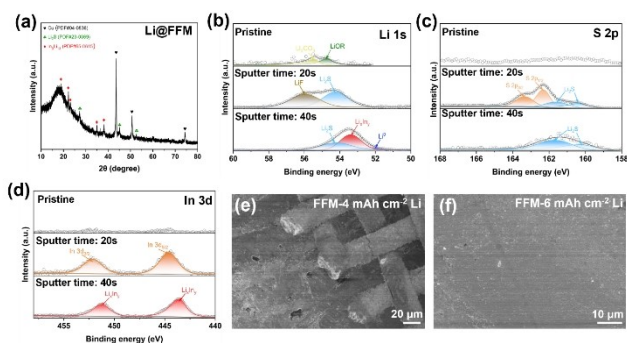
Figure 3. a) XRD pattern of Li@FFM. b) Li_{1s}, c) S_{2p} and d) In_{3d} XPS depth profile of Li@FFM after initial galvanostatic electroplating process. e,f) The corresponding SEM images after Li plating 4, 6 mAh cm^{-2} on FFM.

Figure 4. SEM images of a) Cu net and b) FFM after Li stripping for 4 mAh cm^{-2}. SEM images of the micro-needle treated and subsequent lithium deposition on c) Li@Cu net and d) Li@FFM. e) Cycling performances of symmetric cells with Li@Cu net-needle and Li@FFM-needle at 1 mA cm^{-2} with 1 mAh cm^{-2}. Theoretical investigation of the component properties. f) Li$^+$ adsorption modes of LiIn (111), Li$_3$In$_2$(012), Li$_2$In(100), Li$_{13}$In$_3$(111). g) corresponding Li$^+$ adsorption energy. h) The cyclic voltammograms experiment of FFM at a scan rate of 0.1 mV s^{-1} between 0.01 V and 2.25 V.

nents such as Li_2CO_3 ($\approx 10^{-8}$ S cm^{-1}) and LiF (3×10^{-9} S cm^{-1}), Li_2S has a relatively high ionic conductivity ($\approx 10^{-5}$ S cm^{-1}). This can effectively promote the transport of lithium ions across the entire electrode surface, thereby balancing the kinetic relationship between electrons and lithium ions and enhancing the stability of the electrode/electrolyte interface. Further sputtering revealed the appearance of Li metal (52.4 eV in Li 1s spectra) and LixIny (53.4 eV in Li 1s spectra; 443.6 and 451.2 eV in In 3d spectra), indicating the formation of flexible skeleton during the Li deposition process in the inner layer.

To further investigate the effects of the in-situ formation of intrinsic framework during the lithium deposition process, different amounts of lithium were deposited on FFM (Figure S7, Supporting Information). The cells were then disassembled to observe the anode morphologies by ex situ SEM characterization. As shown in Figure S8 (Supporting Information), following the initial activation process, the establishment of an intrinsic framework has been achieved, and subsequent lithium deposition spreads uniformly across the electrode, achieving a smooth, dense, and dendrite-free lithium deposition morphology (Figure 3e, f).

The morphology of Cu net-stripping can be observed, accompanied by the loss of active material and structure damage (Figure 4a). In sharp contrast, the FFM-stripping maintains structural integrity after lithium deposition and stripping. Combining XRD (Figure S9, Supporting Information) and SEM-Mapping (Figure S10, Supporting Information) analysis, it observed that a small amount of Li_2S and LixIny, namely FFM, stably exist on the surface (Figure 4b), which acts stretchable skeleton role to maintain the structural stability and recover without any residual lithium, indicating desirable structural and plating/stripping reversibility.

To explore the self-healing effect of electrode cracking caused by volume expansion during the lithium deposition and stripping cycles, a 100 μm crack was artificially destroyed into the Li@Cu net (Figure S11, Supporting Information) and Li@FFM (Figure S12, Supporting Information) by micro-needle, which had been deposited with 10 mAh cm^{-2} lithium. Subsequently, 5 mAh cm^{-2} lithium was re-deposited on the damaged electrodes. Comparing the SEM images, it is observed that subsequent lithium deposition on the Li@Cu net-needle (Figure 4c) results
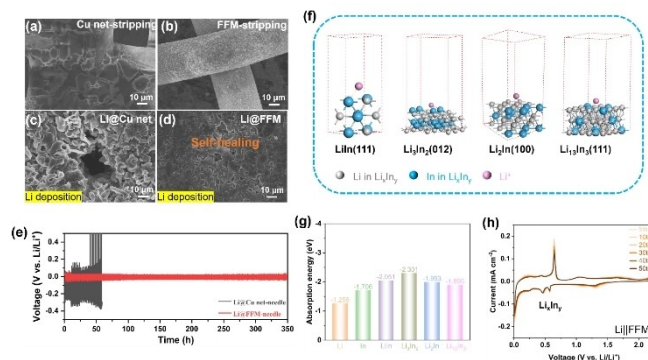
in more disordered accumulation on the surface, exacerbating dendrite formation and the accumulation of "dead lithium". In contrast, during subsequent lithium deposition on the Li@FFM-needle (Figure 4d), the intrinsic framework exhibits an "inside-out" self-healing process, and the subsequent lithium deposition does not result in dendrite formation or "dead lithium" accumulation on the surface. The symmetric cell with Li@FFM-needle electrodes maintains a significantly stable and low overpotential (25 mV) for 350 h at 1 mA cm^{-2} for 1 mAh cm^{-2} Li plating/stripping (Figure 4e). In comparison, the cell based on Li@Cu net-needle exhibits a large overpotential in the initial stage, and after 50 h of cycling, the sharply increased overpotential results in rapid battery failure. These results indicate that the self-healing capability of the intrinsic framework effectively mitigates structural damage to the electrode during lithium deposition/stripping, thereby greatly extending the cycle life.

The adsorption energy of Li$^+$ to Li, In, LiIn, Li$_3$In$_2$, Li$_2$In, and Li$_{13}$In$_3$ were calculated using DFT calculations to investigate the mechanism of lithium deposition on the FFM anode. As presented in Figure 4f, g, the adsorption energy of the most favorable Li approaching site of Li (110) is −1.258 eV which is less negative than that of In (101) (−1.706 eV), LiIn (111) (−2.051 eV), Li$_3$In$_2$ (012) (−2.301 eV), Li$_2$In (100) (−1.993 eV) and Li$_{13}$In$_3$ (111) (−1.895 eV), indicating a greater Li affinity of the LixIny compared to pure Li. From the cyclic voltammetry curves at a scan rate of 0.1 mV s^{-1} between 0.01 V and 2.25 V for the FFM electrode in Figure 4h, it can be observed that the electrode demonstrates improved consistency and repeatability during the lithium deposition/stripping process, which means that the intrinsic framework can function consistently and effectively.

The intrinsic composition distribution of deposited Li on Cu net-In and FFM was further investigated using XPS depth profiles after 400 s of Ar$^+$ sputtering. Overall, the characteristic peaks of Li_2S (54.1 eV in Li$_{1s}$ spectra, Figure 5a; 160.1 and

Batteries & Supercaps

Research Article
doi.org/10.1002/batt.202500033

Chemistry
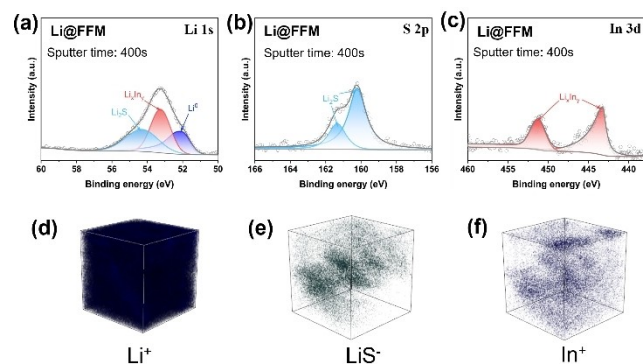Europe
European Chemical
Societies Publishing

Figure 5. Depth profile of a) Li_{1s}, b) S_{2p} and c) In_{3d} XPS spectra Li@Cu net-In and Li@FFM electrode. TOF-SIMS analysis of the 3D distribution of related charged fragments, d) Li^+, e) LiS^-, f) In^+.

Figure 6. a) The voltage-capacity curves of FFM under various current density of 1, 2, 3, 5 mA cm^{-2}. b) Voltage-time curves of symmetric cells using Li@Cu net and Li@FFM at 1 mA cm^{-2} with a capacity of 1 mAh cm^{-2} lithium plating/stripping capacities. c) Coulombic efficiency of Li plating/stripping with areal capacity of 1 mAh cm^{-2} at 1 mA cm^{-2}. EIS spectra of d) Cu net and e) FFM after lithium plating/stripping at a current density of 1 mA cm^{-2} with a capacity of 1 mAh cm^{-2} at the pristine, 25th, 50th, 75th and 100th cycle state. f) Cycling performance of FFM||LFP (red) and Cu net||LFP (black) full cells at a current density of 0.2 C.

161.3 eV in S 2p spectra Figure 5b) and LixIny (53.4 eV in Li 1s spectra Figure 5a; 443.6 and 451.2 eV in In 3d spectra Figure 5c) were observed inside the deposited lithium, originating from the FFM conversions. In contrast, no S or LixIny was detected inside the lithium deposited on the Cu net-In electrode. The LixIny only appears on the surface of the substrate and does not transfer with further lithium deposition, as confirmed by the XPS depth profile (Figure 5a–c) and cross-section SEM-Mapping images of Li@Cu net-In (Figure S13, Supporting Information). 3D tomography with a transverse resolution of 150 μm was employed to investigate the composition and microstructure inside the Li@FFM. As illustrated in Figure 5d–f, ion fragments with mass-to-charge ratios (*m/z*) of 7.02 (Li^+), 38.99 (LiS^-), and 114.92 (In^+) were detected inside the Li@FFM, indicating the presence of intrinsic framework inside the deposited lithium. This was further confirmed by cross-section SEM-Mapping images of Li@FFM (Figure S14, Supporting Information) and TOF-SIMS analysis of the mapping distribution of related elements by depth profiles (Figure S15, Supporting Information).

Based on these characterizations, we can demonstrate that the FFM can be in situ converted into intrinsic framework during the lithium deposition, wherein "expandable molecule chains" are formed through sulfur connections within the deposited lithium. During the lithium stripping process, the flexible chains remain stable, with only their upright state changing. This flexible framework can keep Li striping/plating highly reversibly cycling under 100% DOD.

Subsequently, the nucleation overpotential and deposition overpotentials of different substrates at varying current densities were obtained to evaluate the kinetic acceleration. From the voltage curves at current densities of 1, 2, 3, and 5 mA cm^{-2}, it is observed that the nucleation overpotentials for the Cu net (11.2, 63.3, 166.5, and 244.3 mV, Figure S16, Supporting Information) are significantly higher than FFM anode (Figure 6a), which exhibits almost negligible nucleation overpotential. In addition, the Li||FFM demonstrates lower lithium deposition overpotentials (4.7, 18.3, 34.3, and 67.8 mV) at current densities of 1, 2, 3, and 5 mA cm^{-2} compared with the Li||Cu net (64.1, 116.8, 186.6, and 302.2 mV) (Figure S17, Supporting Informa-
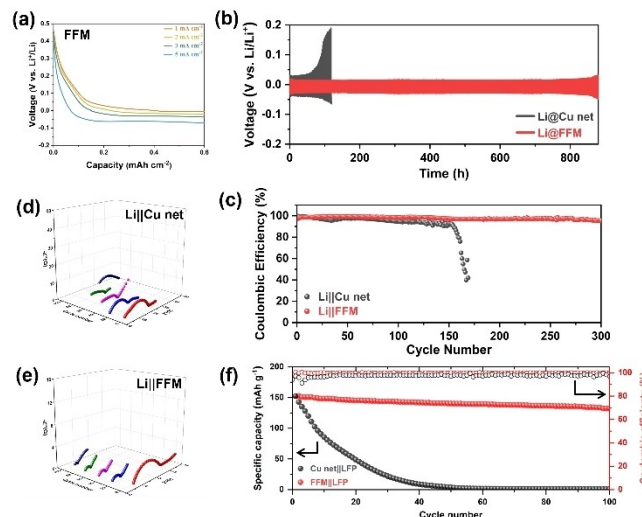
tion). This indicates better ion transport through the Li_2S-enriched interface of Li@FFM compared to the native SEI formed on the Li@Cu net.

Furthermore, the galvanostatic cycling capability and interfacial stability were investigated by repeatedly charging and discharging the symmetric cells at different current densities and capacities. Figure 6b shows the voltage-time profiles for a capacity of 1 mAh cm^{-2} at a current density of 1 mA cm^{-2}. The symmetric cell with Li@FFM electrode remains highly stable and exhibits a low overpotential (16.7 mV) for 800 h (400 cycles). In comparison, the cell based on Li@Cu net shows a large overpotential of 42.1 mV within the initial 80 h (40 cycles), and increases sharply due to battery failure. When the current density is increased to 3 mA cm^{-2} (Figure S18, Supporting Information), Li@FFM maintains a stable voltage of 81.8 mV for 700 h (350 cycles), whereas the Li@Cu net exhibits a sudden overpotential jump to 132.7 mV after 50 h of cycling.

Comparing the CV curves for lithium deposition on Cu net and FFM, it is evident that the initial deposition potential on FFM is positive relative to 0 V (φ_{Li}), indicating underpotential deposition; whereas the deposition potential on Cu net is negative relative to 0 V (φ_{Li}), indicating overpotential deposition occurs (Figure S19, Supporting Information). Additionally, as shown in Figure S20 (Supporting Information), the exchange current density of the Li@FFM electrode (1.96 mA cm^{-2}) in the Tafel curve is higherthan that of the Li@Cu net electrode (0.81 mA cm^{-2}), indicating faster electrode reaction kinetics process.

To evaluate the superiority of the FFM electrode, typical Li||Cu cells, assembled by coupling bare lithium with different electrodes, were subjected to coulombic efficiency (CE) meas-

Batteries & Supercaps

Research Article
doi.org/10.1002/batt.202500033

**Chemistry
Europe**

European Chemical
Societies Publishing

urements. These measurements are crucial parameters for assessing battery cycling reversibility and stability. As shown in Figure 6c, the FFM electrode demonstrates stable electrochemical cycling at various current densities. Specifically, at a current density of 1 mA cm^{-2}, the FFM electrode maintains a stable CE of approximately 98.5% over 300 cycles. In contrast, the cycle life of the Cu net electrode is significantly poorer, with its CE dropping below 80% after only 150 cycles. When the current density is increased to 3 mA cm^{-2}, the FFM electrode achieves a high CE of 97.4% over 200 cycles, while the CE of Cu net decreases sharply after only 30 cycles (Figure S21, Supporting Information). This rapid decline is attributed to the accelerated growth of Li dendrites and the accumulation of "dead Li" on the Cu net.

To reveal the evolution of the electrode interface during the cycling process, EIS tests were further conducted (Figure 6d,e), with the corresponding equivalent circuit model and fitting results shown in Table S1 (Supporting Information). Apparently the ohmic resistance (R_b) and SEI resistance (R_{SEI}) values of FFM remain stable and low throughout the cycling process. In contrast, the R_b and R_{SEI} values of the Cu net grid continued to increase after cycling. The rise in R_b is due to poor electrode contact and low space utilization, while the increase in the R_{SEI} is attributed to the continuous degradation of the SEI layer caused by the disordered growth of lithium dendrites. In addition, we further effectively revealed the details of the electrochemical process through the distribution of relaxation times (DRT) analysis (Figures S28–S29, Supporting Information). By comparison, it can be observed that in the Li||Cu net half-cell, R_b initially decreases and then increases after cycling, while R_{SEI} stabilizes and does not change significantly. This is because the disordered lithium deposition/stripping process on the lithiophobic Cu net substrate tends to cause the accumulation of lithium dendrites and "dead Li" on the electrode surface, thereby affecting the electron transport efficiency on the electrode, resulting in a sharp increase in ohmic impedance. In contrast, in the Li||FFM half-cell, both R_b and R_{SEI} gradually decrease and stabilize at a lower level as cycling progresses, indicating that the regulation of lithium deposition/stripping behavior by FFM can effectively improve the interfacial stability and electron/ion transport efficiency of the electrode. Figure S22–S23 (Supporting Information) also shows the surface morphology SEM images of various electrodes after Li plating/stripping for 100 cycles at a current density of 1 mA cm^{-2} with a capacity of 1 mAh cm^{-2}. The FFM electrode maintains its initial structure without lithium dendrites or "dead lithium", confirming its ideal structural stability and reversible cycling capacity. In sharp contrast, after multiple cycles, a substantial amount of lithium dendrites and "dead lithium" adhere to the surface of the Cu net.

To evaluate the practical application potential, the Cu net and FFM were applied as lithium-free anodes and the LiFePO$_4$ (LFP) was selected as cathodes to assembled full cells, defined as Cu net||LFP and FFM||LFP. In Figure 6f, the FFM||LFP full cell exhibits higher specific capacity of 152.4 mAh g^{-1} at 0.2 C-rate than the Cu net||LFP (specific capacity of 151.0 mAh g^{-1}), indicating severe consumption of Li sources due to the initial

side reactions and loss of active lithium in Cu net. In the subsequent cycles, the FFM||LFP cell shows enhanced cycling performances with capacity retention of 86.7% throughout 100 cycles at 0.2 C-rate. And the Cu net||LFP exhibits severe capacity fading with capacity retention of 32.0% throughout only 20 cycles at 0.2 C-rate. Therefore, inhibiting the generation of "dead lithium" can greatly enhance CE and cycling stability. Moreover, Figure S24–S25 (Supporting Information) displays the voltage profiles of Cu net||LFP and FFM||LFP with different cycles, respectively. The FFM||LFP cell presents almost invariable voltage hysteresis and lower polarization than that of the Cu net||LFP cell, which is attributed to the improved kinetic performance and high Li$^+$ transport efficiency, avoiding the accumulation of by-products at the electrode/electrolyte interface.

Conclusions

In summary, from the perspective of constructing internal functional and support structures, we have developed a functionalized flexible matrix (FFM) for lithium plating/stripping with excellent performance under lithium-free conditions via in-situ conversions. The FFM presents a stretchable molecular chain connected by introduced sulfur which maintains stability and with only upright state changes during the lithium dissolution and deposition process, thus serving as a flexible skeleton to self-supporting lithium plating/stripping, leading to a smooth and dense dendritic-free lithium deposition pattern. Benefiting from these attributes, the AFLMB FFM||LFP exhibited superior Coulombic efficiency and high capacity of 88.7% retention at 0.2 C-rate after 100 cycles. All these above advantages suggest that our study provides a promising strategy for regulating the lithium dissolution and deposition process to develop high-energy-density and high-cycle-stability rechargeable anode-free lithium metal batteries.

Conflict of Interests

The authors declare no conflict of interest.

Data Availability Statement

The data that supported the findings of this study are available from the corresponding author upon reasonable request.

[1] D. Luo, M. Li, Q. Y. Ma, G. B. Wen, H. Z. Dou, B. H. Ren, Y. Z. Liu, X. Wang, L. L. Shui, Z. W. Chen, *Chem. Soc. Rev.* **2022**, *51*, 2917.

[2] Y. S. Tian, G. B. Zeng, A. Rutt, T. Shi, H. Kim, J. Y. Wang, J. Koettgen, Y. Z. Sun, B. Ouyang, T. N. Chen, Z. Y. Lun, Z. Q. Rong, K. Persson, G. Ceder, *Chem. Rev.* **2021**, *121*, 1623.

[3] X. B. Cheng, R. Zhang, C. Z. Zhao, Q. Zhang, *Chem. Rev.* **2017**, *117*, 10403.

[4] S. Park, H. J. Jin, Y. S. Yun, *Adv. Mater.* **2020**, *32*, 22.

[5] Y. Xia, Y. Jiang, Y. Y. Qi, W. Q. Zhang, Y. Wang, S. F. Wang, Y. M. Liu, W. W. Sun, X. Z. Zhao, *J. Power Sources* **2019**, *442*, 10.

[6] X. Y. Zhang, A. X. Wang, X. J. Liu, J. Y. Luo, *Acc. Chem. Res.* **2019**, *52*, 3223.

[7] D. H. Liu, Z. Y. Bai, M. Li, A. P. Yu, D. Luo, W. W. Liu, L. Yang, J. Lu, K. Amine, Z. W. Chen, *Chem. Soc. Rev.* **2020**, *49*, 5407.

[8] J. Liu, Z. N. Bao, Y. Cui, E. J. Dufek, J. B. Goodenough, P. Khalifah, Q. Y. Li, B. Y. Liaw, P. Liu, A. Manthiram, Y. S. Meng, V. R. Subramanian, M. F. Toney, V. V. Viswanathan, M. S. Whittingham, J. Xiao, W. Xu, J. H. Yang, X. Q. Yang, J. G. Zhang, *Nat. Energy* **2019**, *4*, 180.

[9] J. J. Pan, K. X. Shi, H. Wu, J. H. Li, R. Zhang, Q. B. Liu, Z. X. Liang, *Adv. Energy Mater.* **2023**, 10.

[10] S. Cho, D. Y. Kim, J. I. Lee, J. Kang, H. Lee, G. Kim, D. H. Seo, S. Park, *Adv. Funct. Mater.* **2022**, *32*, 11.

[11] Z. Q. Li, X. L. Huang, L. Kong, N. Qin, Z. Y. Wang, L. H. Yin, Y. Z. Li, Q. M. Gan, K. M. Liao, S. Gu, T. F. Zhang, H. Huang, L. N. Wang, G. F. Luo, X. Cheng, Z. G. Lu, *Energy Storage Mater.* **2022**, *45*, 40.

[12] S. Pyo, S. Ryu, Y. J. Gong, J. Cho, H. Yun, H. Kim, J. Lee, B. Min, Y. Choi, J. Yoo, Y. S. Kim, *Adv. Energy Mater.* **2023**, *13*, 12.

[13] B. L. Wu, C. G. Chen, L. H. J. Raijmakers, J. Liu, D. L. Danilov, P. H. L. Notten, *Energy Storage Mater.* **2023**, *57*, 508.

[14] B. A. Jote, T. T. Beyene, N. A. Sahalie, M. A. Weret, B. W. Olbassa, Z. T. Wondimkun, G. B. Berhe, C. J. Huang, W. N. Su, B. J. Hwang, *J. Power Sources* **2020**, *461*, 7.

[15] A. J. Louli, A. Eldesoky, R. Weber, M. Genovese, M. Coon, J. deGooyer, Z. Deng, R. T. White, J. Lee, T. Rodgers, R. Petibon, S. Hy, S. J. H. Cheng, J. R. Dahn, *Nat. Energy* **2020**, *5*, 693.

[16] H. Choi, Y. Bae, S. M. Lee, Y. C. Ha, H. C. Shin, B. G. Kim, *J. Electrochem. Sci. Technol.* **2022**, *13*, 78.

[17] N. A. Sahalie, A. A. Assegie, W. nN. Su, Z. T. Wondimkun, B. A. Jote, B. Thirumalraj, C. J. Huang, Y. W. Yang, B. J. Hwang, *J. Power Sources* **2019**, *437*, 226912.

[18] R. Weber, M. Genovese, A. J. Louli, S. Hames, C. Martin, I. G. Hill, J. R. Dahn, *Nat. Energy* **2019**, *4*, 683.

[19] T. M. Hagos, G. B. Berhe, T. T. Hagos, H. K. Bezabh, L. H. Abrha, T. T. Beyene, C. J. Huang, Y. W. Yang, W. N. Su, H. Dai, B. J. Hwang, *Electrochim. Acta* **2019**, *316*, 52.

[20] Z. Tong, B. Bazri, S.-F. Hu, R.-S. Liu, *J. Mater. Chem. A* **2021**, *9*, 7396.

[21] L. Su, H. Charalambous, Z. Cui, A. Manthiram, *Energy Environ. Sci.* **2022**, *15*, 843.

[22] Z. T. Wondimkun, T. T. Beyene, M. A. Weret, N. A. Sahalie, C. J. Huang, B. Thirumalraj, B. A. Jote, D. Wang, W. N. Su, C. H. Wang, G. Brunklaus, M. Winter, B. J. Hwang, *J. Power Sources* **2020**, *450*, 227589.

[23] S. Menkin, C. A. O'Keefe, A. B. Gunnarsdottir, S. Dey, F. M. Pesci, Z. Shen, A. Aguadero, C. P. Grey, *J. Phys. Chem. C* **2021**, *125*, 16719.

[24] A. Shao, X. Tang, M. Zhang, M. Bai, Y. Ma, *Adv. Energy Sustain. Res.* **2022**, *3*, 2100197.

[25] Y. Tian, Y. An, C. Wei, H. Jiang, S. Xiong, J. Feng, Y. Qian, *Nano Energy* **2020**, *78*, 105344.

[26] C. Heubner, S. Maletti, H. Auer, J. Hüttl, K. Voigt, O. Lohrberg, K. Nikolowski, M. Partsch, A. Michaelis, *Adv. Funct. Mater.* **2021**, *31*, 2106608.

[27] A. J. Louli, A. Eldesoky, J. deGooyer, M. Coon, C. P. Aiken, Z. Simunovic, M. Metzger, J. R. Dahn, *J. Electrochem. Soc.* **2022**, *169*, 040517.

[28] J. Zhang, H. Chen, M. Wen, K. Shen, Q. Chen, G. Hou, Y. Tang, *Adv. Funct. Mater.* **2022**, *32*, 2110110.

[29] L. Lin, L. Suo, Y. S. Hu, H. Li, X. Huang, L. Chen, *Adv. Energy Mater.* **2021**, *11*, 2003709.

[30] A. A. Assegie, C. C. Chung, M. C. Tsai, W. N. Su, C. W. Chen, B. J. Hwang, *Nanoscale* **2019**, *11*, 2710.

[31] V. Pande, V. Viswanathan, *ACS Energy Lett.* **2019**, *4*, 2952.

[32] X. Wang, Y. He, S. Tu, L. Fu, Z. Chen, S. Liu, Z. Cai, L. Wang, X. He, Y. Sun, *Energy Storage Mater.* **2022**, *49*, 135.

[33] J. Chen, J. Xiang, X. Chen, L. Yuan, Z. Li, Y. Huang, *Energy Storage Mater.* **2020**, *30*, 179.

[34] X. Y. Cui, J. C. Cheng, C. Li, Z. Q. Sun, K. X. Li, Y. J. Wang, X. X. Fan, S. Tang, X. D. Lin, R. M. Yuan, B. W. Mao, M. S. Zheng, Q. F. Dong, *Energy Environ. Mater.* **2023**, *6*, 9.

[35] J. N. Duan, Q. Hou, R. M. Yuan, J. M. Fan, M. S. Zheng, Q. F. Dong, *J. Mater. Chem. A* **2023**, *11*, 548.

[36] Y. M. Chen, X. Ke, Y. F. Cheng, M. P. Fan, W. L. Wu, X. Y. Huang, Y. H. Liang, Y. C. Zhong, Z. M. Ao, Y. Q. Lai, G. X. Wang, Z. C. Shi, *Energy Storage Mater.* **2020**, *26*, 56.

[37] C. Yan, R. Xu, Y. Xiao, J. F. Ding, L. Xu, B. Q. Li, J. Q. Huang, *Adv. Funct. Mater.* **2020**, *30*, 21.

[38] X. Y. Liu, P. Xu, J. L. Zhang, X. Y. Hu, Q. Hou, X. D. Lin, M. S. Zheng, Q. F. Dong, *Small* **2021**, *17*, 10.

[39] S. S. Zhang, X. Fan, C. Wang, *Electrochim. Acta* **2017**, *258*, 1201–1207.

[40] X. Wang, Y. He, S. Tu, L. Fu, Z. Chen, S. Liu, Z. Cai, L. Wang, X. He, Y. Sun, *Energy Storage Mater.* **2022**, *49*, 135–143.

[41] Z. T. Wondimkun, T. T. Beyene, M. A. Weret, N. A. Sahalie, C. J. Huang, B. Thirumalraj, B. A. Jote, D. Wang, W. N. Su, C. H. Wang, G. Brunklaus, M. Winter, B. J. Hwang, *J. Power Sources* **2020**, *450*, 227589.

[42] Z. T. Wondimkun, W. A. Tegegne, J. Shi Kai, C. J. Huang, N. A. Sahalie, M. A. Weret, J. Y. Hsu, P. L. Hsieh, Y. S. Huang, S. H. Wu, W. N. Su, B. J. Hwang, *Energy Storage Mater.* **2021**, *35*, 334–344.

[43] H. Liu, X. Yue, X. Xing, Q. Yan, J. Huang, V. Petrova, H. Zhou, P. Liu, *Energy Storage Mater.* **2021**, *16*, 505–511.

[44] S. K. Merso, T. M. Tekaligne, H. H. Weldeyohannes, Y. Nikodimos, K. N. Shitaw, S. K. Jiang, C. J. Huang, Z. T. Wondimkun, B. A. Jote, L. Wichmann, G. Brunklaus, M. Winter, S. H. Wu, W. N. Su, C. Y. Mou, B. J. Hwang, *J. Energy Storage* **2022**, *56*, 105955.

[45] S. Cho, D. Y. Kim, J. I. Lee, J. Kang, H. Lee, G. Kim, D. H. Seo, S. Park, *Adv. Funct. Mater.* **2022**, *32*, 2208629.

[46] S. Koul, Y. Morita, F. Fujisaki, H. Ogasa, Y. Fujiwara, A. Kushima, *J. Electrochem. Soc.* **2022**, *169*, 020542.